MODELING OF THE EXCITED MODES IN INVERTED EMBEDDED MICROSTRIP LINES USING THE FINITE-DIFFERENCE TIME-DOMAIN (FDTD) TECHNIQUE

A Thesis
Presented to
The Academic Faculty

By

Amil Haque

In Partial Fulfillment
of the Requirements for the Degree
Master of Science in the
School of Electrical and Computer Engineering

Georgia Institute of Technology
December 2008

MODELING OF THE EXCITED MODES IN INVERTED EMBEDDED MICROSTRIP LINES USING THE FINITE-DIFFERENCE TIME-DOMAIN (FDTD) TECHNIQUE

Approved by:

Dr. Emmanouil M. Tentzeris, Advisor
School of Electrical and Computer Engineering
Georgia Institute of Technology

Dr. Andrew F. Peterson
School of Electrical and Computer Engineering
Georgia Institute of Technology

Dr. Ioannis Papapolymerou
School of Electrical and Computer Engineering
Georgia Institute of Technology

Dr. Joy Laskar
School of Electrical and Computer Engineering
Georgia Institute of Technology

Date Approved: November 14, 2008

ACKNOWLEDGEMENTS

Firstly, I would like to thank my parents, my eldest brother, and my wife, for their guidance, love, and support. I would also like to thank my graduate advisor, Dr. Manos Tentzeris for his advice and help. I am very grateful to the thesis committee consisting of Dr. John Papapolymerou, Dr. Joy Laskar, and Dr. Andrew Peterson for reviewing my work. Lastly, I would like to thank NASA for funding this project.

TABLE OF CONTENTS

LIST OF TABLES

LIST OF FIGURES

LIST OF SYMBOLS AND ABBREVIATIONS

FDTD	finite-difference time-domain
3-D	three-dimensional
2.5-D	two-and-a-half dimensional
TEM	Transverse Electromagnetic

SUMMARY

This thesis investigates the presence of multiple (quasi-TEM) modes in inverted embedded microstrip lines. It has already been shown that parasitic modes do exist in inverted embedded microstrips due to field leakage inside the dielectric substrate, especially for high dielectric constants (like Silicon) [1]. This thesis expands upon that work and characterizes those modes for a variety of geometrical dimensions.

Chapter 1 focuses on the theory behind the different transmission line modes, which may be present in inverted embedded microstrips. Based on the structure of the inverted embedded microstrip, the conventional microstrip mode, the quasi-conventional microstrip mode, and the stripline mode are expected.

Chapter 2 discusses in detail the techniques used to decompose the total probed field into the various modes present in the inverted embedded microstrip lines. Firstly, a short explanation of the finite-difference time-domain method, that is used for the simulation and modeling of inverted microstrips up to 50 GHz is provided. Next, a flowchart of the process involved in decomposing the modes is laid out. Lastly, the challenges of this approach are also highlighted to give an appreciation of the difficulty in obtaining accurate results.

Chapter 3 shows the results (dispersion diagrams, values/percentage of the individual mode energies) obtained after running time-domain simulations for a variety of geometrical dimensions.

Chapter 4 concludes the thesis by explaining the results in terms of the transmission line theory presented in Chapter 1. Next, possible future work is mentioned.

CHAPTER 1

INTRODUCTION

1.1 Motivation

Inverted microstrips have gained popularity over the last decade in novel 3D microwave structures due to their inherent advantages of lower loss and smaller overall structure size. For example, inverted microstrip lines permit the use of defected ground structures (DGS) [2] on Silicon substrates. Typically, a DGS on low-resistivity silicon would have high loss, but by using inverted microstrip topologies, the silicon conductivity will not degrade its performance [2]. Inverted microstrip lines have also been used in Liquid Crystal (LC) phase shifters, where the LC material is used as the filling between the upper ground plane and the strip, resulting in smaller size, lighter weight, and low cost [3]. Plus, inverted microstrip lines have been widely utilized in numerous implementations of flip-chip packaging. In this case, the MMIC is fabricated as a normal microstrip line, but when flipped onto the carrier substrate (eg. InP), the topology is converted to an inverted microstrip [4]. Finally, inverted microstrip lines have been embedded in between different layers of dielectrics, such as polyimide, for ultra high-speed applications [5]. Unfortunately, despite some preliminary theoretical efforts showing some evidence of parasitic modes [1], no thorough investigation has been performed on the properties of these modes, something required before they are widely incorporated into novel embedded structures, involving Monolithic Microwave Integrated Circuits (MMICs), in order to predict parasitic coupling and leakage effects.

Experimental measurements made on inverted embedded microstrips have shown

that they do not exhibit the same dispersion characteristics with conventional microstrip transmission lines (mostly the quasi-TEM microstrip mode), due to the higher leakage of electromagnetic fields into the high dielectric-constant (e.g. Si) substrate [1].

The purpose of this thesis is to characterize all these modes related to the inverted embedded microstrips. Firstly, 2.5-D FDTD simulations will be run with field probes placed at various locations, and in particular at those places where the peaks of modes are expected. It is expected that apart from the conventional microstrip mode found in regular microstrip transmission lines, there will also be energy coupling to other modes present in the structure. Next, 2.5D/3D FDTD simulations will be run to obtain field patterns for the various modes. It is expected that one will be able to visually verify the assumption of the higher order modes from the field patterns produced. Lastly, 3D FDTD simulations will be run to estimate the relative amplitude of individual mode power values (as a percentage fraction of the total-power).

1.2 Modes Analysis for Printed Transmission Lines

1.2.1 Geometry

The purpose of this section is to identify the possible modes present in an inverted embedded microstrip by comparing them to modes which propagate in conventional printed transmission lines that have been already thoroughly investigated and studied by the scientific community (e.g. the Quasi-TEM microstrip mode present in microstrip line geometries, and the TEM mode present in stripline geometries).

Without loss of generality, the benchmarked Inverted Embedded Microstrip geometry consists of a microstrip line that is embedded into 4 layers of polyimide which

are stacked on top of each other with individual layer thicknesses of 2.5μm, with the ground metal at the top layer (Figure 1 [1]).

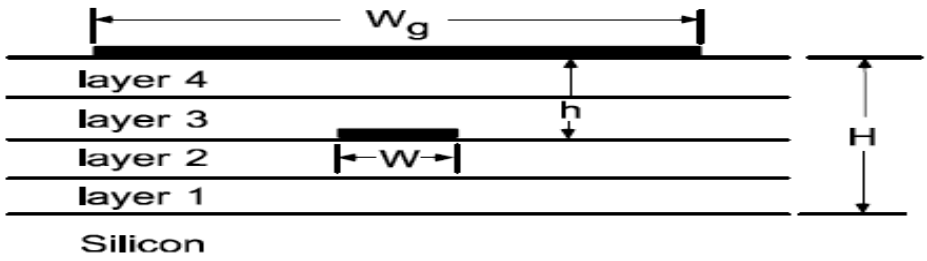

Figure 1. 2-D cross-section view of inverted embedded microstrip line

The height of the polyimide layer (H) is 10μm, and the height of the Silicon layer is 529μm. The ground width (W_g), microstrip line width (W) and the distance between the microstrip line and ground are adjusted so that the input impedance of the microstrip line is 50 Ω (Table 1 [1]).

Table 1: Dimensions of embedded inverted microstrip lines

Layer	h(μm)	W (μm)	W_g (μm)
1	7.5	11	55
2	5.0	9	45
3	2.5	5	25

The polyimide layer has a dielectric constant of 3.12, and the silicon substrate has a dielectric constant of 11.9. Both dielectrics are considered to be lossless for simulation purposes.

Figure 1 shows that the inverted embedded microstrip line does show some structural similarity to a conventional microstrip line in terms of both having a microstrip (signal) line and a ground plane. The next section discusses how the modes of an inverted embedded microstrip line can be predicted by comparing it to the modes found within a conventional microstrip line.

1.2.2 Microstrip quasi-TEM mode

A microstrip transmission line consists of a conductor of width W printed on a thin, grounded dielectric substrate of thickness d as shown in Figure 2 [6].

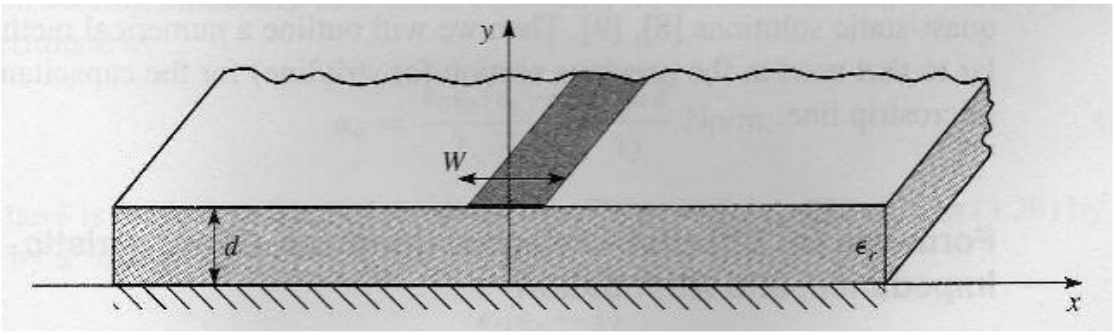

Figure 2. Microstrip transmission line geometry

If there was no substrate of thickness d present between the two metal lines and their width was the same in the topology of Figure 2, then the microstrip transmission line would be similar to a parallel plate transmission line which supports a simple TEM mode with $v_p = c$ and $\beta = k_0$ (v_p is the phase velocity, c is the speed of light, β is the

propagation constant, and k_0 is the wave number in free space). However, the presence of the substrate leads to two different phase velocities in the substrate region and in the air. Hence, a quasi-TEM mode is present with the majority of the field lines confined in the dielectric substrate [6]. Figure 3 below shows the electric and magnetic field lines in a conventional microstrip structure [6].

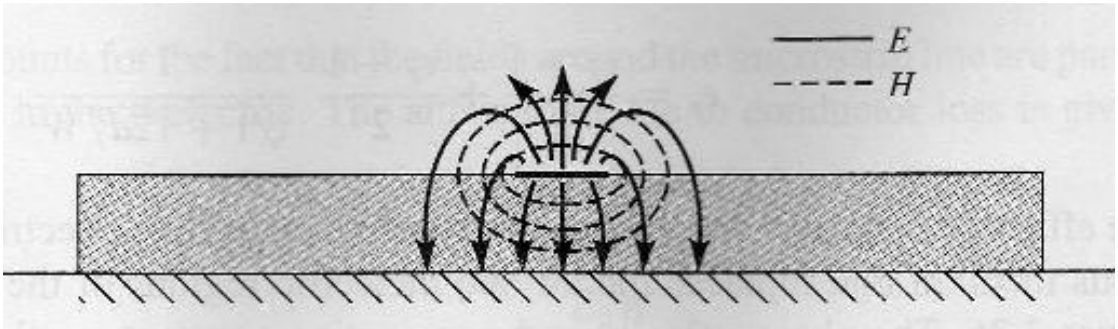

Figure 3. Microstrip Transmission line Electric and Magnetic field lines.

Since some of the field lines are in the dielectric region and some are in air, this leads to an effective dielectric constant with a value between the dielectric constant of air and the dielectric constant of the substrate. Now, the propagation constant of the quasi-TEM mode can be expressed as follows:

$$\beta = k_0 \sqrt{\varepsilon_{eff}} \tag{1}$$

Figure 4 below shows the evolution from a conventional microstrip line to an inverted embedded transmission line. Firstly, when a finite-ground conventional microstrip is embedded in a layer of dielectric (Figure 4(b)), the majority of the fields which were leaking into the air (Figure 4(a)), now leak into a higher permittivity dielectric. This would increase the effective permittivity of the conventional microstrip

mode. Next, when the ground plane of an embedded microstrip line is shortened from infinite (Figure 4(b)) to finite (Figure 4(c)), there is fringing of fields from the edge of the finite ground plane into the Si substrate [7]. Experimental data shows that if the finite ground is reduced to a size above 3 times the microstrip width, the fringing fields can be ignored [7]. Finally, if the positions of the microstrip line and ground are switched (Figure 4(c) to Figure4(d)), then there is leakage of electric fields into the high dielectric constant Silicon substrate. This will additionally increase the effective relative permittivity of the conventional microstrip mode. Hence, in going from a conventional microstrip line to an inverted embedded microstrip line, the basic conventional microstrip mode is still excited.

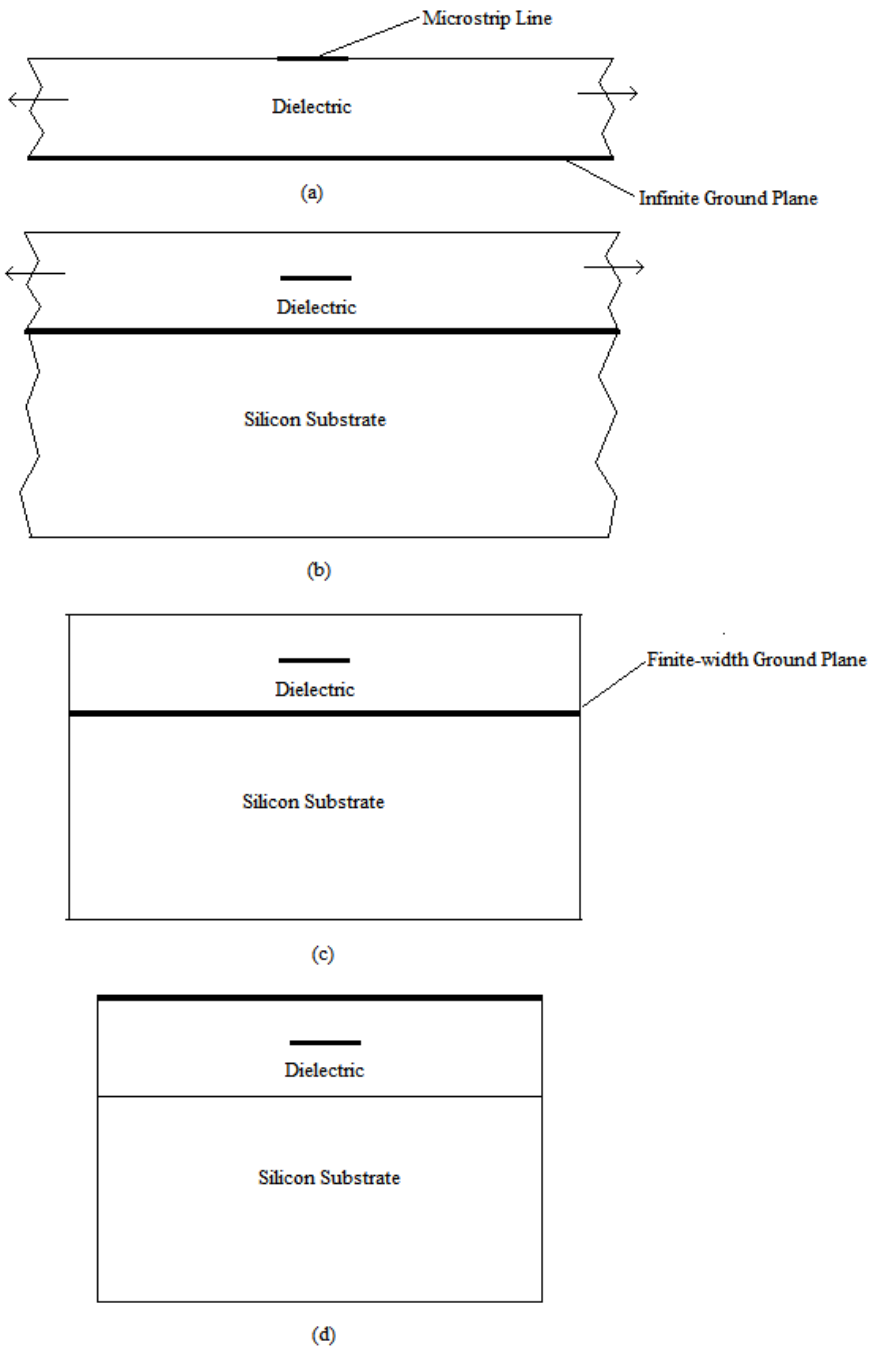

Figure 4. (a) Conventional Microstrip Transmission Line
(b) Embedded Microstrip Transmission Line
(c) Finite-Ground Embedded Microstrip Transmission Line
(d) Finite-Ground Inverted Embedded Transmission Line

It is also proposed that another quasi-TEM microstrip mode exists between the microstrip line and the dielectric interface between the polyimide and Silicon interface, that could function as an imperfect conductor, effectively limiting the leakage of the electric lines.

The reflection coefficient at the boundary of the interface can be approximated by Equation 2, because the majority of the electric field intensity is normal to the direction of the dielectric interface.

$$\Gamma = \frac{|E_r|}{|E_i|} = \frac{\eta_2 - \eta_1}{\eta_2 + \eta_1} \tag{2}$$

where $|E_i|$ is the magnitude of the incident electric field, $|E_r|$ is the magnitude of the reflected Electric field, η_1 is the intrinsic impedance of the substrate in which the incident field propagates, and η_2 is the intrinsic impedance of the medium in which the transmitted field propagates, where η is the intrinsic impedance of a material, and is given by:

$$\eta = \sqrt{\frac{\mu}{\varepsilon}} \tag{3}$$

In this dielectric interface, there is a large difference between the permittivity of Silicon (11.9) and the permittivity of polyimide (3.12), which makes the reflection coefficient at the dielectric interface very high. This means there is almost total reflection, making this interface a "non-ideal PEC". Another reason this interface has a high reflection coefficient is that the conductivity of the Silicon interface is much higher than that of the polyimide interface, hence the Silicon appears as a 'metal' with respect to the polyimide.

The above two modes will exist mainly inside the polyimide layer. The latter

mode, the quasi TEM microstrip mode between the microstrip line and the dielectric interface, will have a higher effective permittivity because the dielectric interface is not a perfect PEC and does allow some energy to leak into the higher permittivity Silicon layer.

Since both of these modes are quasi-TEM, the equation describing their propagation constant will be very close to the one for a conventional microstrip quasi-TEM mode shown in Equation 1 ($\beta = k_0\sqrt{\varepsilon_{eff}}$) featuring an almost linear dependence on the frequency. The dispersion diagram is not exactly a straight line because the microstrip line is dispersive and at higher frequencies the effective dielectric constant tends to approach the dielectric constant of the substrate [8],[9].

1.2.3 Stripline mode

A stripline transmission line consists of a thin conducting strip of width W centered between two wide conducting ground planes of separation, with the entire region between the ground planes filled with a dielectric. In practice, stripline is usually constructed by etching the center conductor on a grounded substrate of thickness b/2 and then covering with another grounded substrate of the same thickness [6]. An example of a stripline circuit is shown in Figure 5 [6].

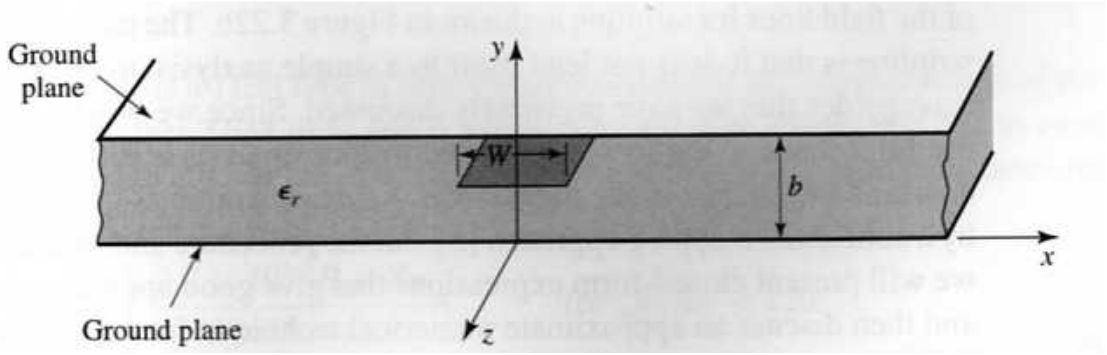

Figure 5. Stripline transmission line geometry

Since stripline has two conductors and a homogeneous dielectric, it can support a TEM wave, and this is the usual mode of operation [6]. Figure 6 below shows the electric and magnetic field lines in a stripline structure [6].

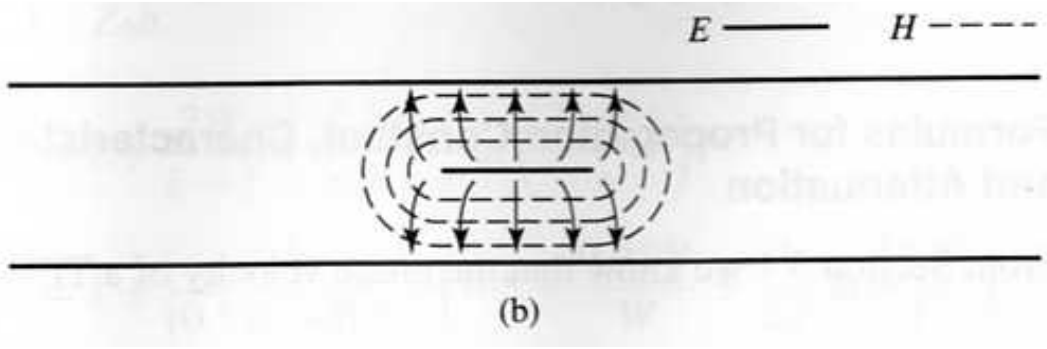

Figure 6. Stripline Transmission line Electric and Magnetic field lines

There are two differences between the stripline mode of the stripline and the quasi-stripline mode of the inverted embedded transmission line. Firstly, the inverted embedded transmission line has a finite width ground, which would behave almost like an infinite ground width only in the case that the ground width is at least 3-5 times the

width of the microstrip line. Secondly, there is only one metal layer, and the second metal layer is replaced by a 'metal-like' polyimide-Silicon interface which has been described previously.

1.4 Summary

Chapter I focused on the theory behind the different kinds of transmission line modes which may be present in an inverted embedded microstrip. Based on the structure of the inverted embedded microstrip, the conventional microstrip mode, quasi-conventional microstrip mode, and stripline mode are expected. Although the ideal mode distributions (conventional microstrip and stripline) are perturbed, a possible explanation for their existence is that the Silicon-polyimide interface behaves like a metal plane.

CHAPTER 2

METHODOLOGY

2.1 Finite-Difference Time-Domain (FDTD)

2.1.1 3-D FDTD

This section describes the different methods used to solve Maxwell's Equations computationally. The Finite Difference Time domain is a method which was formulated by Yee in 1961 to solve Maxwell's curl Equations. It employs a leapfrog scheme where the electric and magnetic fields are interleaved on a unit cell and the whole structure is synthesized utilizing these cells. In this thesis, we utilized a Cartesian grid made of cubic unit cell, similar to the one shown in Figure 7.

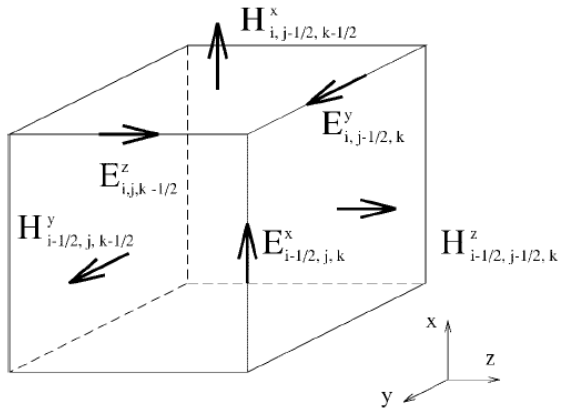

Figure 7. Yee's FDTD cell

Yee's FDTD scheme discretizes the curl Maxwell equations by approximating the time and space first-order partial derivatives with centered differences. For example, the H-field is given by:

$$H_x^{n+0.5}(i,j+1/2,k+1/2) - H_x^{n-0.5}(i,j+1/2,k+1/2) =$$
$$\frac{\Delta t}{\mu_0}\left(\frac{E_y^n(i,j+1/2,k+1) - E_y^n(i,j+1/2,k)}{\Delta z} - \frac{E_z^n(i,j+1,k+1/2) - E_z^n(i,j,k+1/2)}{\Delta y}\right)$$

$$H_y^{n+0.5}(i+1/2,j,k+1/2) - H_y^{n-0.5}(i+1/2,j,k+1/2) =$$
$$\frac{\Delta t}{\mu_0}\left(\frac{E_z^n(i+1,j,k+1/2) - E_z^n(i,j,k+1/2)}{\Delta x} - \frac{E_x^n(i+1/2,j,k+1) - E_x^n(i+1/2,j,k)}{\Delta z}\right) \quad (4)$$

$$H_z^{n+0.5}(i+1/2,j+1/2,k) - H_z^{n-0.5}(i+1/2,j+1/2,k) =$$
$$\frac{\Delta t}{\mu_0}\left(\frac{E_x^n(i+1/2,j+1,k) - E_x^n(i+1/2,j,k)}{\Delta y} - \frac{E_y^n(i+1,j+1/2,k) - E_y^n(i,j+1/2,k)}{\Delta x}\right)$$

The equations for the *E*-field are discretized similarly, and are dual in nature. The intervals: Δx, Δy, Δz, and Δt represent the unit space interval in the *x*-, *y*-, *z*-direction, and the unit time interval, respectively. The indexes *i*, *j*, *k*, and *n* are related to the space and time coordinates via $x=i\Delta x$, $y=j\Delta y$, $z=k\Delta z$, and $t=n\Delta t$ [10],[11].

2.1.2 2.5-D FDTD

Although the FDTD method is a versatile and robust method for solving most electromagnetic field problems, one commonly known disadvantage of the FDTD if utilized in frequency selective analysis problems is, that it requires large amounts of memory space and CPU time, in particular for the full-wave analysis of hybrid modes in quasiplanar circuits or in inhomogeneous waveguide structures [12]. A solution to this problem was proposed by introducing a Novel 2-D FDTD mesh with reduced grid size (as compared to 3-D FDTD), for the analysis of arbitrarily shaped guided wave structures [12].

The new approach modifies the two-step leapfrog FDTD procedure initially developed for a three dimensional grid. After the field components are normalized by the

the free space impedance $Z_0 = \sqrt{\mu_0 / \varepsilon_0}$ [12]:

$$\begin{aligned} E^n_{x,y,z}(i,j,k) &= e^n_{x,y,z}(i,j,k)\sqrt{Z_0} \\ H^{n+0.5}_{x,y,z}(i,j,k) &= h^{n+0.5}_{x,y,z}(i,j,k)/\sqrt{Z_0} \end{aligned} \tag{5}$$

one obtains [12]

$$\begin{aligned} h_x^{n+0.5}(i,j,k) &= h_x^{n-0.5}(i,j,k) - s\{(e_z^n(i,j,k) - e_z^n(i,j+1,k) - e_y^n(i,j,k+1) + e_y^n(i,j,k)\} \\ h_y^{n+0.5}(i,j,k) &= h_y^{n-0.5}(i,j,k) - s\{(e_x^n(i,j,k+1) - e_x^n(i,j,k) - e_z^n(i+1,j,k) + e_z^n(i,j,k)\} \\ h_z^{n+0.5}(i,j,k) &= h_z^{n-0.5}(i,j,k) - s\{(e_y^n(i+1,j,k) - e_y^n(i,j,k) - e_x^n(i,j+1,k) + e_x^n(i,j,k)\} \\ e_x^{n+1}(i,j,k) &= e_x^n(i,j,k) + s\{(h_z^{n+0.5}(i,j,k) - h_z^{n+0.5}(i,j-1,k) - h_y^{n+0.5}(i,j,k) + h_y^{n+0.5}(i,j,k-1)\} \\ e_y^{n+1}(i,j,k) &= e_y^n(i,j,k) + s\{(h_x^{n+0.5}(i,j,k) - h_x^{n+0.5}(i,j,k-1) - h_z^{n+0.5}(i,j,k) + h_z^{n+0.5}(i-1,j,k)\} \\ e_z^{n+1}(i,j,k) &= e_z^n(i,j,k) + s\{(h_y^{n+0.5}(i,j,k) - h_y^{n+0.5}(i-1,j,k) - h_x^{n+0.5}(i,j,k) + h_x^{n+0.5}(i,j-1,k)\} \end{aligned} \tag{6}$$

where $s = c\Delta t / \Delta h$ is the stability condition, and i,j, and k, are the indices along the x,y, and z direction respectively, and where Δh is the uniform cell size in the direction of propagation.

When the modes have been established after a transient period of time following the excitation, only a phase shift $\beta\Delta h$ is involved at any adjacent node along the direction of propagation for any specific propagation constant β. This modal knowledge is now used to simplify the scheme. It is easy to see that any incident or reflected field impulse for any propagation constant β satisfies [12]:

$$\begin{aligned} e_p^n(i,j,k \pm 1) &= e_p^n(i,j,k)\exp\{\mp j\beta\Delta h\} \\ h_p^n(i,j,k \pm 1) &= h_p^n(i,j,k)\exp\{\mp j\beta\Delta h\}, \end{aligned} \quad p = x, y, \tag{7}$$

then (6) can be written as (8) [12].

$$
\begin{aligned}
h_x^{n+0.5}(i,j) &= h_x^{n-0.5}(i,j) - s\{(e_z^n(i,j+1) - e_z^n(i,j) + 2\sin(\beta\Delta h/2)e^{j(\pi-\beta\Delta h)/2}e_y^n(i,j)\} \\
h_y^{n+0.5}(i,j) &= h_y^{n-0.5}(i,j) - s\{(e_z^n(i,j) - e_z^n(i+1,j) + 2\sin(\beta\Delta h/2)e^{j(\pi-\beta\Delta h)/2}e_x^n(i,j)\} \\
h_z^{n+0.5}(i,j) &= h_z^{n-0.5}(i,j) - s\{(e_y^n(i+1,j) - e_y^n(i,j) - e_x^n(i,j+1) + e_x^n(i,j)\} \\
e_x^{n+1}(i,j) &= e_x^n(i,j) + s\{(h_z^{n+0.5}(i,j) - h_z^{n+0.5}(i,j-1) - 2\sin(\beta\Delta h/2)e^{j(\pi-\beta\Delta h)/2}h_y^{n+0.5}(i,j)\} \\
e_y^{n+1}(i,j) &= e_y^n(i,j) + s\{(h_z^{n+0.5}(i-1,j) - h_z^{n+0.5}(i,j) - 2\sin(\beta\Delta h/2)e^{j(\pi-\beta\Delta h)/2}h_x^{n+0.5}(i,j)\} \\
e_z^{n+1}(i,j) &= e_z^n(i,j) + s\{(h_y^{n+0.5}(i,j) - h_y^{n+0.5}(i-1,j) - h_x^{n+0.5}(i,j) + h_x^{n+0.5}(i,j-1)\}
\end{aligned}
\tag{8}
$$

where Δt is the time step. In this way the 3-D FDTD grid can be reduced to an "enhanced" 2-D cross section where the z-direction can be considered to have "collapsed" (Figure 8) [12].

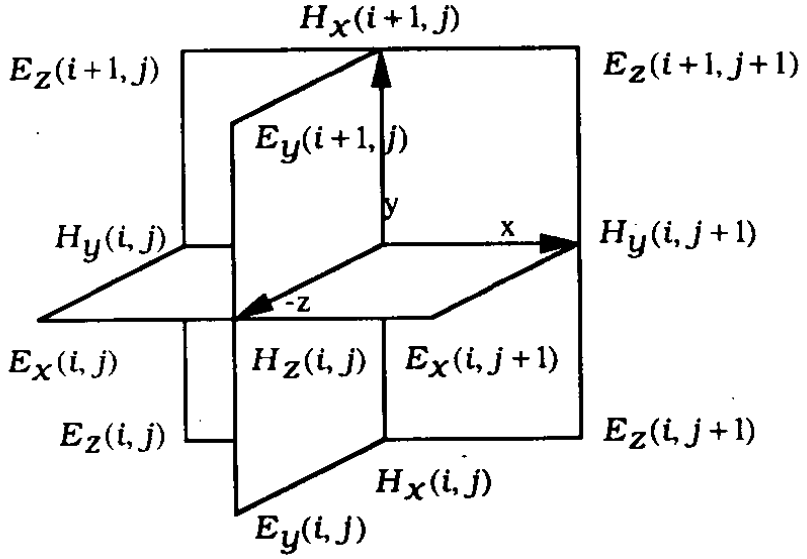

Figure 8. Novel 2-D FDTD mesh, with "collapsed" z-direction

The grid size in z-direction is arbitrary as long as the transmission line is homogeneous in this direction [12].

To find the frequencies at which modes are excited in a structure, a propagation constant is selected and the structure is excited with a time-domain impulse. Next, a

fourier transform is taken over the frequency range of operation of the structure. Each peak in the frequency spectrum corresponds to a particular mode. This step must then be repeated for different propagation constants to obtain the dispersion curve for one particular mode [12]. Further steps are then required to identify field distributions for different modes; these are discussed in Section 2.3.

2.2 Discretization

This section describes how the inverted embedded microstrip line is modeled with 2.5D simulations (Refer to Figure 9.). The width of the microstrip line in the horizontal direction is 4 cells, and the width of the ground plane in the horizontal direction is 20 cells. Each cell is in the order of a thousandth of the effective wavelength in length. Such a small discretization is required because the width of the microstrip line is in the order of μm, and several cells are required to represent it so that there is a good resolution of the electric and magnetic fields when mode decomposition is performed. This satisfies the usual discretization requirement of the cell size being below one twentieth of the wavelength. Due to the concentrated nature of the field lines, there were no absorbing boundaries used in this setup, but, instead, PEC boundaries were placed at a certain distance from the circuit as shown in Figure 9. If the PEC is too close to the circuit large reflections from the PEC boundary will affect the mode behavior, but the further the PEC boundaries are from the microstrip line the longer the simulation time will be. The vertical and horizontal distance of the PEC boundary from the microstrip ground is adjusted to minimize computation time and maintain good accuracy. It is found that this occurs when the PEC boundary is 1440μm (32 ground-widths) away from the ground plane in the horizontal direction and 360μm (36 polyimide-heights) away

from the ground plane in the vertical direction. A large grid is required so that the complete mode distribution can be captured and so that radiated energy reaching the PEC boundaries falls to at least -60dB in magnitude, making any reflection from the PEC boundary negligible.

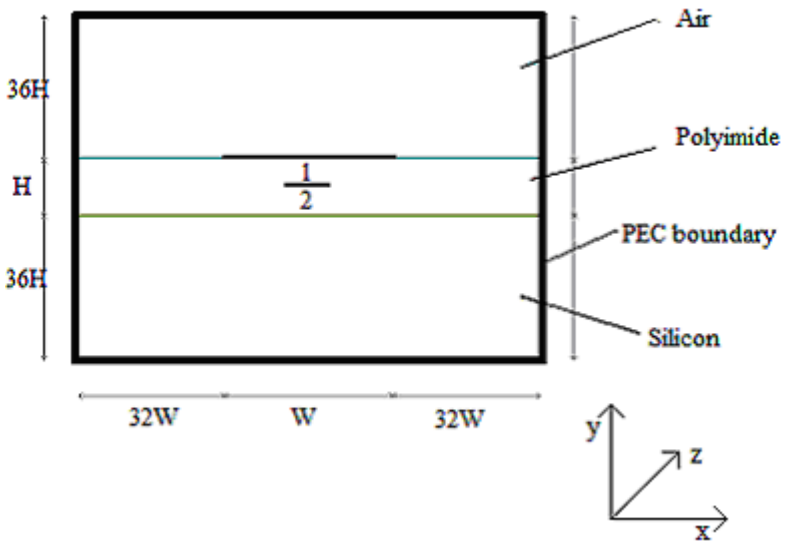

Figure 9. 2-D cross-section view of schematic used for 2.5-D FDTD simulation

2.3 Separation/Decomposition of modes

Firstly, 2.5-D FDTD simulations were run from beta = 200 to beta = 2000 for this topology with field probes placed at various locations, and in particular at those places where the peaks of modes are expected. These peaks are expected at those locations where the maximum electric field occurs. For the quasi-TEM mode which propagates between the microstrip line and the ground the maximum electric field is near probe 1 (Figure 9), and for the quasi-TEM mode which propagates between the microstrip line and the dielectric interface the maximum electric field is near probe 2 (Figure 9). For the

quasi-stripline TEM mode which propagates between the microstrip line, the ground, and the 'metal-like' polyimide-silicon interface the, maximum electric field would be near probe 1 or probe 2 (Figure 9).

Three excitations are used. The first excitation is a delta pulse (value equal to 1) at all points between ground and signal at time t = 0 - aiming to excite the conventional microstrip mode, the second excitation is a delta pulse at all points lying between the Polyimide/Silicon dielectric interface and the microstrip signal line at time t = 0 - aiming to excite the parasitic quasi-TEM quasi-microstrip mode, and the third excitation is two delta pulses at time t=0, one at all points between ground and signal, and the other at all points lying between the Polyimide/Silicon dielectric interface and the microstrip signal line - aiming to excite the quasi-stripline TEM mode. Figure 10 below shows the location of these excitations for all three cases.

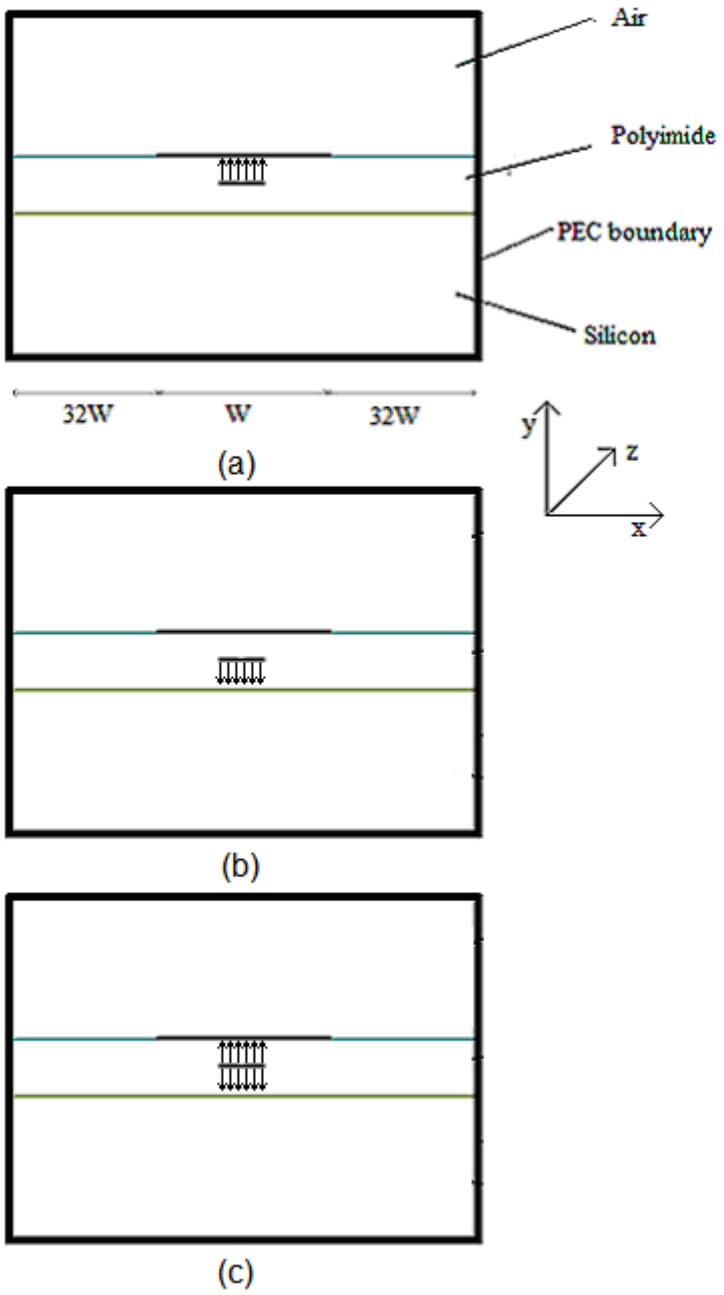

Figure 10. (a) Excitation region to excite the quasi-TEM mode between the microstrip line and ground
(b) Excitation region to excite the quasi-TEM mode between the microstrip line and Silicon/Polyimide dielectric interface
(c) Excitation region to excite the quasi-stripline TEM mode

In all three cases, an FFT window from 0 to 60 GHz is chosen so that all frequencies in this range are excited. The three excitations described above could potentially excite a parallel-plate TEM mode between the microstrip line and ground, and higher-order TE as well as TM parallel-plate modes, but the frequency range of interest guaranteed that we are below their cutoff frequencies. The first higher order parallel plate (TE1/TM1) mode is found to in the order of 10THz using Eq. 10, which is much higher than our frequency range of interest.

$$f_c = \frac{n}{2d\sqrt{\mu\varepsilon}} \tag{10}$$

Assuming all modes are quasi-TEM (something verified by simulations for ten different β values), the value of ε_{eff} can be easily determined by $\beta=2\pi f*(\mu_0*\varepsilon_0*\varepsilon_{eff})^{1/2}$ [13], where f is the resonant frequency of each mode. The resonant frequency of each mode corresponds to a peak in the frequency spectrum. Using this information a dispersion diagram for each mode can also be constructed. Next, new 2.5-D FDTD simulations are run to obtain 2-D cross sectional field patterns applying FFT for the resonant frequencies of 10GHz, 20GHz, 30GHz, 40GHz, and 50GHz, for all three excitations mentioned previously. The propagation constant (β) corresponding to each of the resonant frequencies 10GHz, 20GHz, 30GHz. 40GHz, 50GHz, can be found by interpolation of the dispersion diagram of the mode of interest. By observing the field patterns it is possible to identify the modes. Then, the electromagnetic fields of each mode are modified such that the total power transmitted by each mode is 1W. This is achieved by dividing the electric and magnetic fields by the square root of the magnitude of the complex power (surface integral of the power vector over the cross-section of the structure). Since the modified electric and magnetic fields have their magnitudes reduced

by the square root of the complex power, when the magnitude of the complex power of the adjusted field values is taken it will be 1W (If ρ is the magnitude of the complex power, then $\iint(\vec{E}_{t-orig} \times \vec{H}^{*}_{t-orig})dxdy = \rho$, (where the subscript 't' refers to the transverse field components) and if $\vec{E}_{t-\mathrm{mod}} = \frac{\vec{E}_{t-orig}}{\sqrt{\rho}}$ (where the subscript 'mod' refers to a modified field value), and $\vec{H}_{t-\mathrm{mod}} = \frac{\vec{H}_{t-orig}}{\sqrt{\rho}}$, then $\iint(\vec{E}_{t-\mathrm{mod}} \times \vec{H}^{*}_{t-\mathrm{mod}})dxdy = \frac{\rho}{\sqrt{\rho} * \sqrt{\rho}} = 1W$).

Lastly, a 3-D FDTD simulation is run with a soft source Gaussian pulse vertical excitation with f_{max} = 60GHz close to the front end of the microstrip. Next, 2-D cross sectional composite-mode electromagnetic field patterns are taken by applying FFT at 10GHz, 20GHz, 30GHz, 40GHz, and 50GHz; these are five frequencies we would like to investigate the mode decomposition at. Next, the cross-sectional composite-mode patterns are modified so that the magnitude of the total complex power transmitted by the composite mode is 1W. This is achieved by dividing the field values by the square root of the magnitude of the complex modal power as explained previously. To find the percentage power carried by a single mode at each one of the five frequencies, the magnitude of the cross product of the Electric field vector from the 3-D derived mode pattern is performed with the conjugate of the Magnetic field vector from the 2.5-D simulation at that frequency for each normalized cross-sectional mode of the 2.5-D simulation over the full domain of simulation [14] and squared . Equation 9 shows this formulation, where the subscript 'mod' refers to a modified electric or magnetic field:

$$\left|\iint\left(E_{x3D-\mathrm{mod}}\cdot H^{*}_{y2.5D-\mathrm{mod}}-E_{y3D-\mathrm{mod}}\cdot H^{*}_{x2.5D-\mathrm{mod}}\right)dxdy\right|^{2} x100 \qquad (9)$$

Equation 9 gives the percentage mode power because by taking the magnitude of the cross product of the 3-D modified electric field with the magnetic field from the 2.5-D simulation over the area of simulation, essentially the ratio of the modified 2.5-D mode magnetic field to the modified 3-D magnetic field is obtained; then by squaring this number we get the percentage mode power because the ratio of powers is the ratio of the fields squared (Lastly this number is multiplied by 100 to give a percentage). This procedure is repeated for each mode of interest to find the percentage power carried by each mode. Lastly, this procedure is repeated for different values of h (Refer to Table 1). Figure 11 shows a flowchart which summarizes this process.

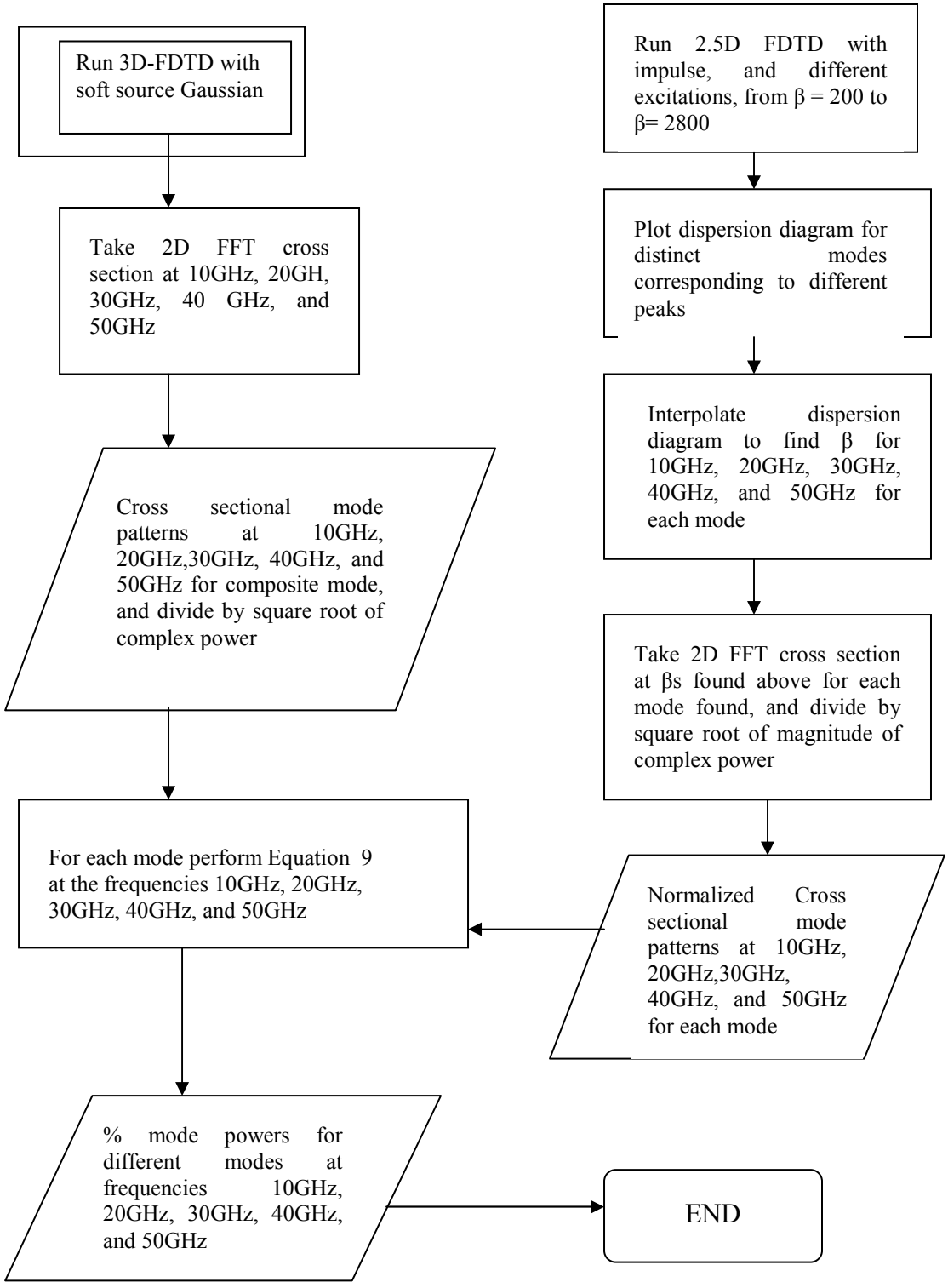

Figure 11. Flowchart summarizing process used to find percentage power of each propagating mode

2.4 Summary

Chapter 2 provided an explanation of the methods used to decompose the various modes present in the inverted embedded microstrip geometries.

CHAPTER 3

SIMULATION RESULTS

3.1 Separation/Decomposition of modes

3.1.1 Visual identification of modes

After a 3-D FDTD simulation is run with a soft source Gaussian pulse, and a 2-D cross sectional composite-mode electromagnetic field patterns is taken by applying FFT, the Magnitude of the total electric field ($|\vec{E}| = \sqrt{(|E_x|^2 + |E_y|^2}$) along the cross section of the microstrip line for the composite-mode is found to confine most of the electric field between the microstrip line and ground. Figure 12 shows $|\vec{E}|$ at 30GHz for the composite-mode.

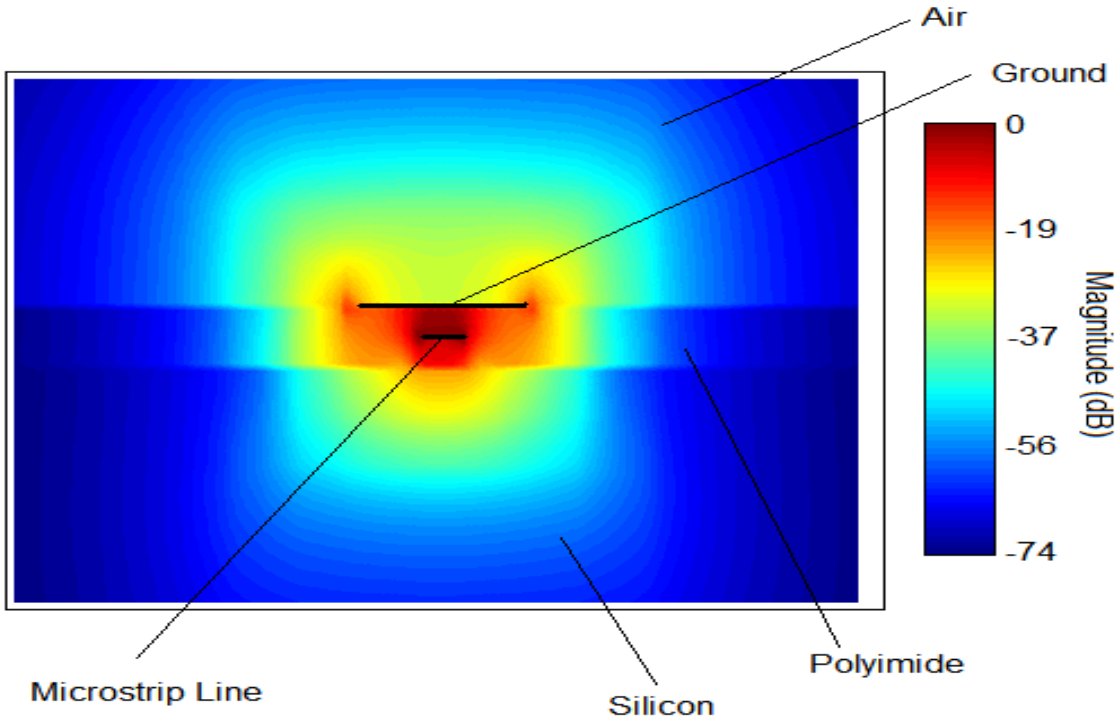

Figure 12. 2-D cross-section view of $|\vec{E}|$ at 30GHz from 3-D simulation

Next, 2.5D-FDTD simulation are run from β = 200rad/m to β = 2800rad/m, using the 3 excitations described in the previous section. After taking the FFT, it is found for each value of β that 2 peaks are found at the same frequencies, for each of the excitation cases. This implies that there are only two distinct modes propagating within the inverted embedded transmission line, and not three as surmised earlier. Then the FFT is applied for each mode pattern along the cross section to find the total electric field distribution. It was found that the first mode was a quasi-TEM mode between the microstrip line and ground, because it confined most the electric field between the microstrip line and ground, and that the second mode was a quasi-TEM mode between the microstrip line and Silicon/Polyimide interface because it confined most of the electric field between the microstrip line and Silicon/Polyimide interface. Figure 13 is a plot of $\left|\vec{E}\right|$ at 30GHz for these 2 modes. The next section shows the dispersion diagram which was plotted by selecting the frequency peaks from the simulations run from from β = 200rad/m to β = 2800rad/m.

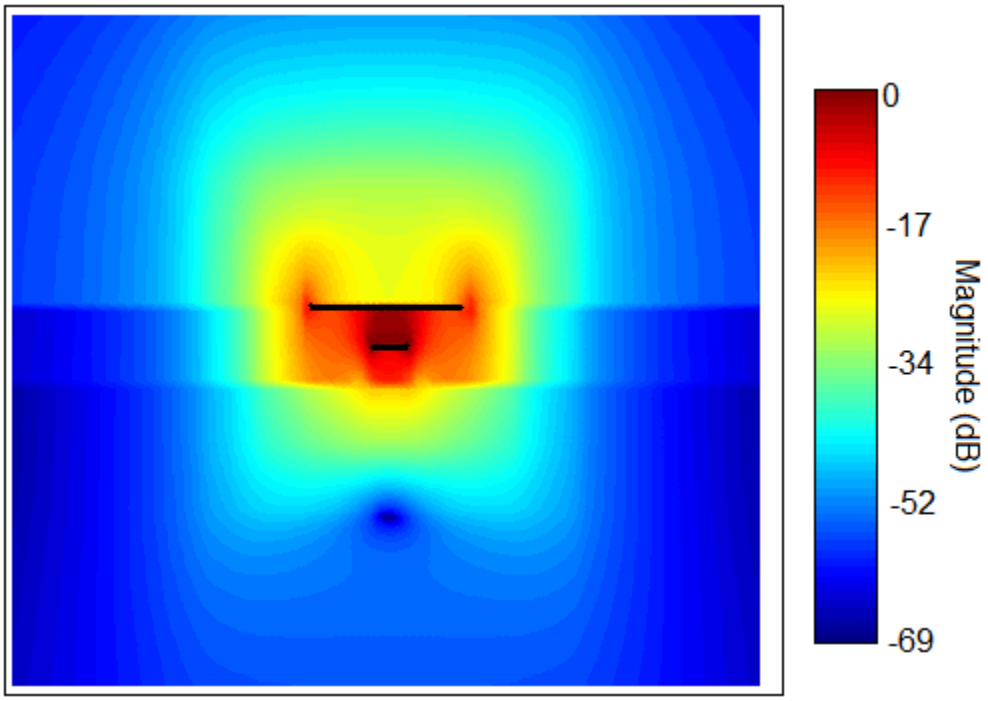

(a)

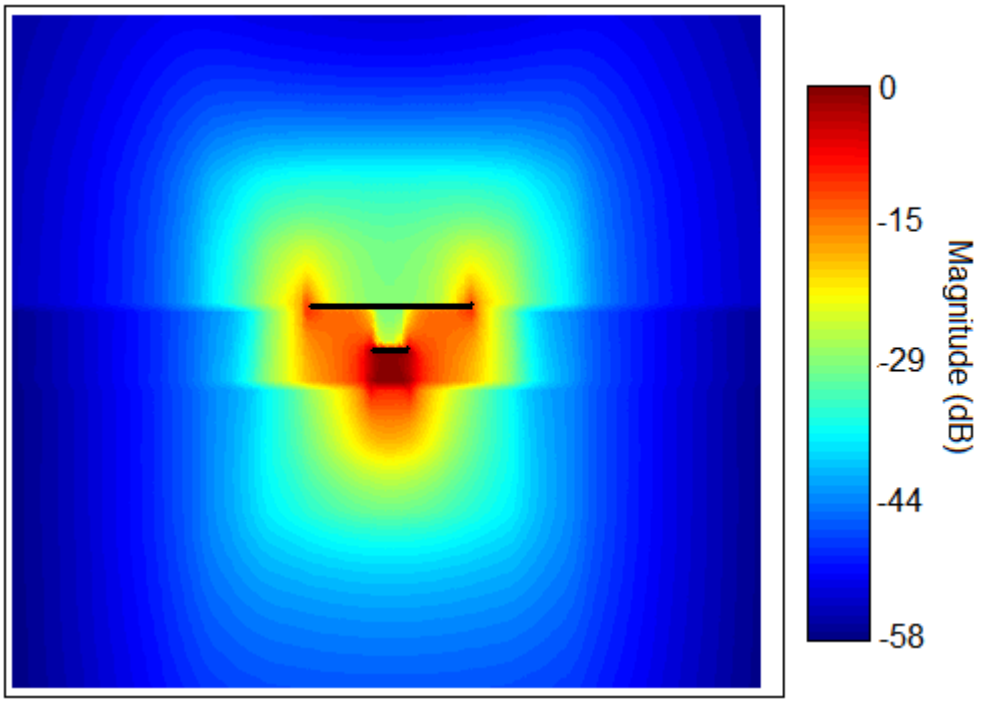

(b)

Figure 13. 2-D cross-section view of $|\vec{E}|$ at 30GHz for (a) quasi-TEM mode between microstrip line and ground and (b) quasi-TEM mode between microstrip line and Silicon/Polyimide dielectric interface

3.1.2 Dispersion Diagram

After selecting the position of the frequency peaks from the 2.5D-FDTD simulations from β = 200rad/m to β = 2800rad/m, a dispersion diagram was plotted for the two modes which were found to propagate. The first mode is a quasi-TEM mode from the microstrip line to the ground plane (Figure 13(a)) with an effective dielectric constant of 3.21 ($\beta = k_0\sqrt{\varepsilon_{eff}}$) for h = 5μm, and the second mode is a quasi-TEM mode from the microstrip line to the dielectric interface (Figure 13(b)) with an effective dielectric constant of 4.98 ($\beta = k_0\sqrt{\varepsilon_{eff}}$) for h = 5μm. The dispersion diagram for both modes are found to be nearly straight lines (Figure 14), verifying our assumption of quasi-TEM modes. The next section describes the mode percentage power obtained after performing the mode decomposition, for various frequencies and values of h.

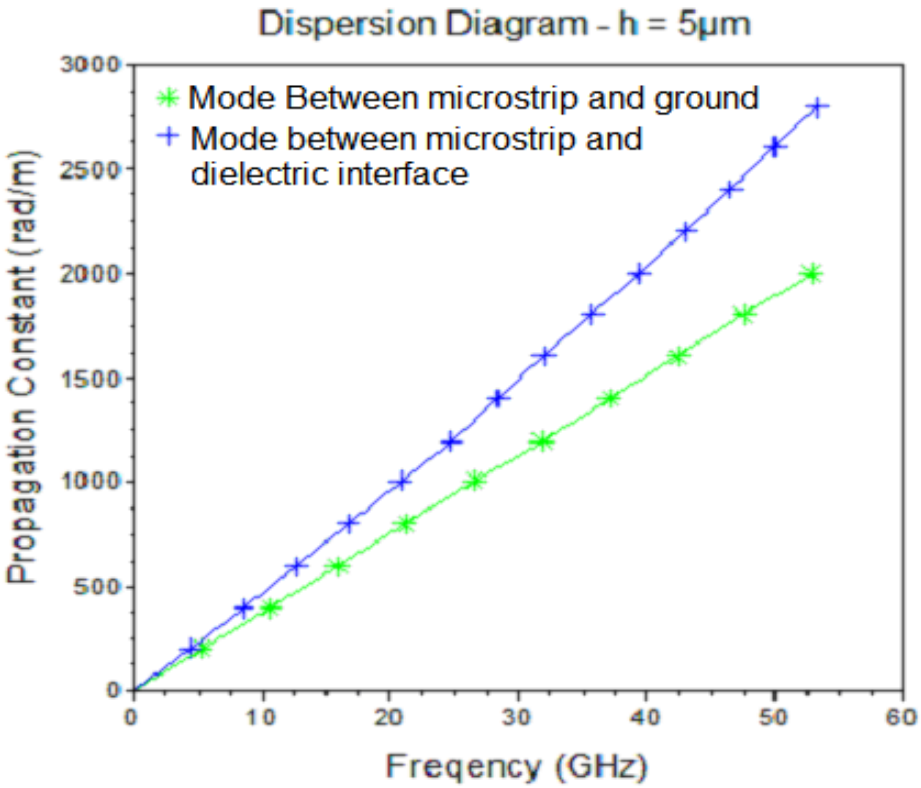

Figure 14. Dispersion diagram for h = 5µm of inverted embedded microstrip (Table 1)

3.1.3 Mode Powers

By using the method outlined in the flowchart of Figure 11, the percentage of power carried by each mode at different frequencies and vales of h (Refer to Table 1) was calculated. Varying the value of h, it was found that the mode amplitudes and dielectric constants vary as shown in Table 2 (where h refers to the distance between the microstrip line and ground plane (Please Refer to Table 1 for the corresponding microstrip dimensions), m1 refers to the quasi-TEM mode between the microstrip line and ground, and m2 refers to the quasi-TEM mode between the microstrip line and dielectric interface.

Table 2: Mode Properties as h is varied

Freq (GHz)	**h = 7.5**μm m1	**h = 7.5**μm m2	**h = 5.0**μm m1	**h = 5.0**μm m2	**h = 2.5**μm m1	**h = 2.5**μm m2
10	89.1	10.9	93.1	6.9	94.8	5.2
20	90.3	9.7	94.3	5.7	96.7	3.3
30	93.2	6.8	95.6	4.4	97.4	2.6
40	94.2	5.8	96.5	3.5	97.5	2.5
50	95.2	4.8	97.7	2.3	98.3	1.7
$\varepsilon_{eff\ (average)}$	**3.40**	**5.58**	**3.21**	**4.98**	**3.06**	**4.30**

It was found that by decreasing the value of h, more electromagnetic energy gets confined in a smaller region, thus increasing the power carried by m1. Also, ε_{eff} decreases because now more of the field is confined within the polyimide layer, whose dielectric constant is 3.12 and less energy leaks into the Silicon layer, whose dielectric constant is 11.8. This can be observed in Figure 15 which shows the 2D cross section view of $\left|\vec{E}\right|$ at 30GHz at different h.

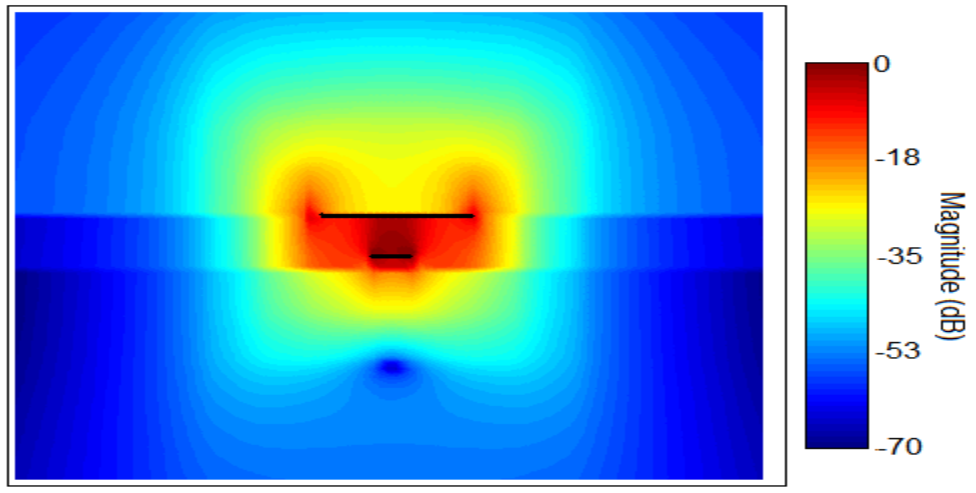

h = 7.5μm

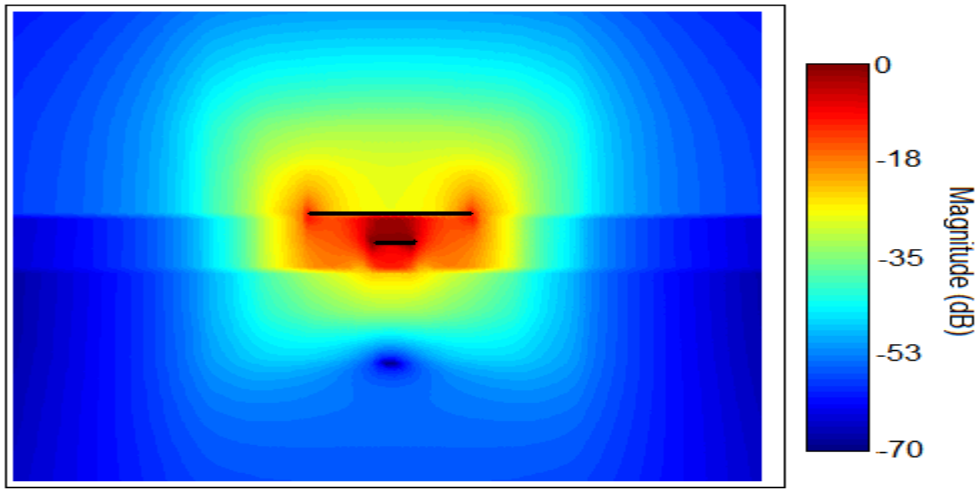

h = 5μm

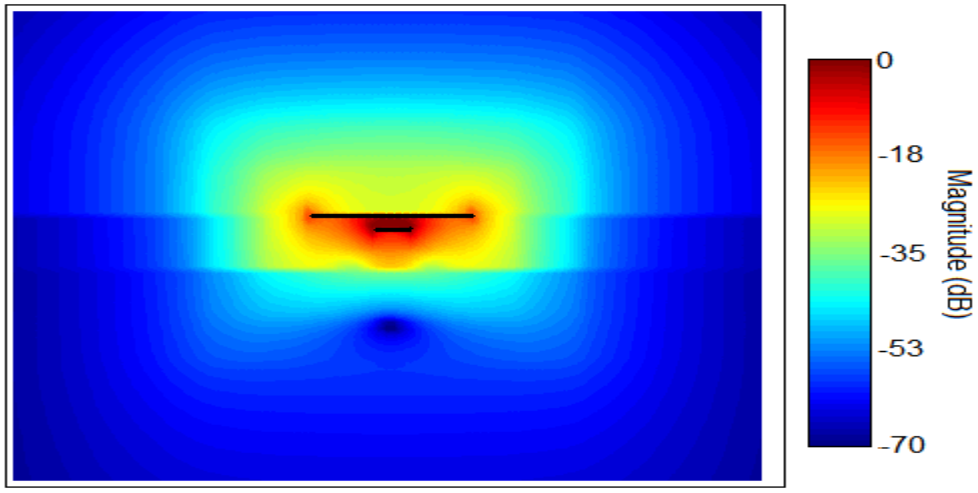

h = 2.5μm

Figure 15. 2-D cross-section view of $|\vec{E}|$ at 30GHz for m1 after varying h

With regards to m2, as the value of h is decreased less energy is concentrated between the micrsotrip line and the Silicon/Polyimide interface, thus decreasing the power carried by it. Figure 16 illustrates why ε_{eff} decreases. As h is decreased, more energy resides in the polyimide and air region compared to the Silicon region, which brings down the ε_{eff} to a lower value. As h is decreased ε_{eff} for m1 decreases at a slower rate than that of m2, because in the case of m1 the leakage of electromagnetic fields into the Silicon layer decreases at a slower rate(as h is decreased) than m2.

As the frequency is increased from 10GHz to 50GHz, the amplitude of m1 is found to increase, and the amplitude of m2 is found to decrease. This is because increasing the frequency decreases the wavelength, which causes the electrical length between the microstrip line and ground to decrease. This in turn decreases the effective spacing between the microstrip line and ground, causing the amplitude of m1 to increase.

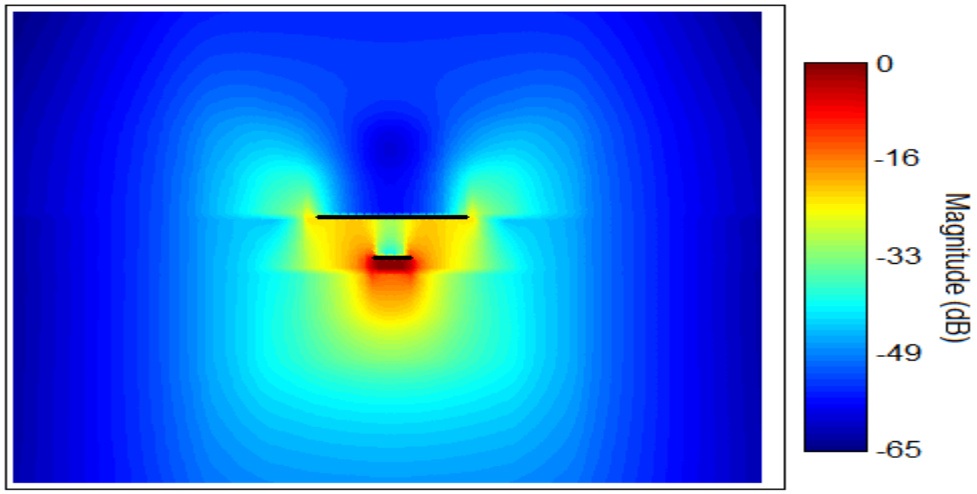

h = 7.5μm

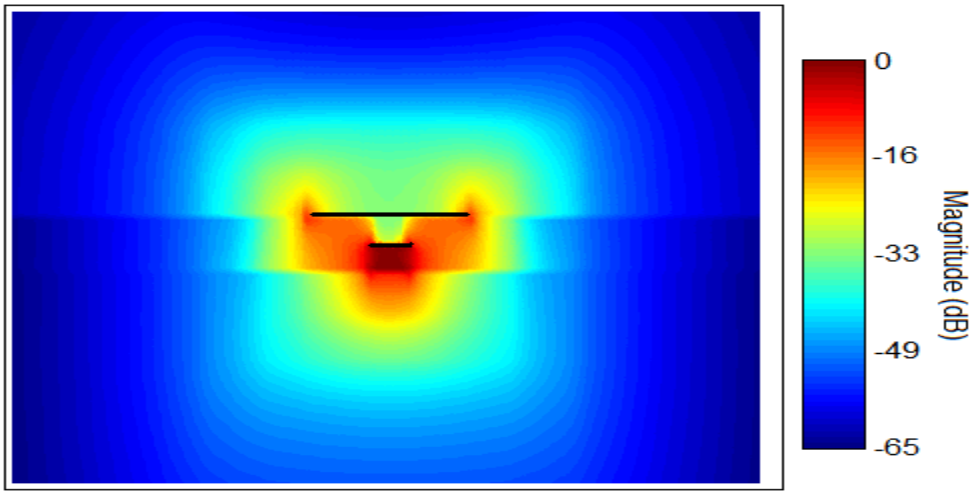

h = 5.0μm

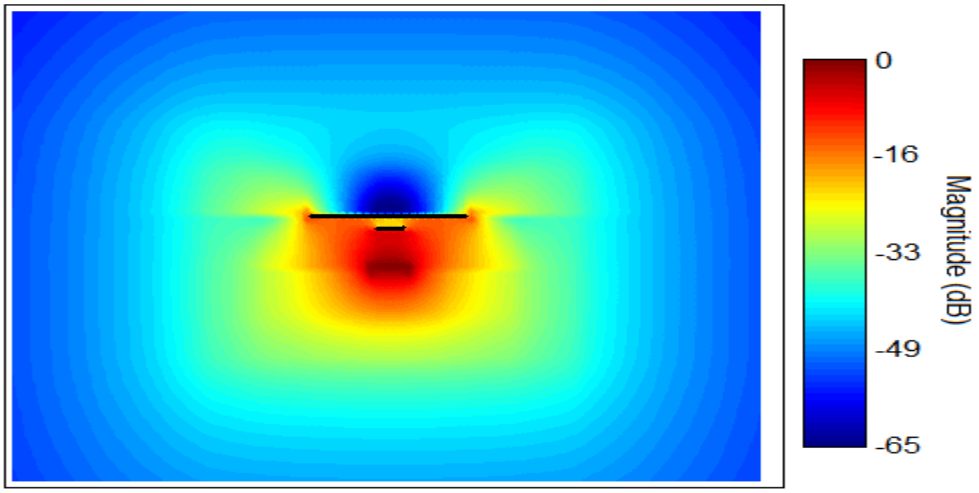

h = 2.5μm

Figure 16. 2-D cross-section view of $|\vec{E}|$ at 30GHz for m2 after varying h

3.2 Summary

Chapter III shows the results obtained after running simulations. The dispersion diagram and mode energies of the various modes are shown. There are two modes found to propagate at all frequencies: a quasi-TEM mode between microstrip line and ground, and a quasi-TEM mode between microstrip line and Silicon/Polyimide dielectric interface.

CHAPTER 4

CONCLUSION

The modes of an inverted embedded microstrip are decomposed and characterized. The quasi-TEM mode between microstrip line and ground has an ε_{eff} that is close to 3, which means that most of the energy is confined within the polymide region, whereas the quasi-TEM mode between the ground and Silicon/Polyimide interface has a higher $\varepsilon_{eff,}$ which means that there is some leakage of electromagnetic fields into the Silicon substrate that pushes its dielectric constant higher. There was no quasi-stripline TEM mode found.

CHAPTER 5

FUTURE WORK

Future work could involve investigation on how to reduce the unwanted quasi-TEM mode between the microstrip line and Silicon/Polyimide dielectric interface. Another area to investigate is to simulate Silicon with high resistivity and check if the mode amplitudes are affected.

REFERENCES

[1] PONCHAK, G. E., and TENTZERIS, M. M., "Multiple modes on embedded inverted micrsotrips," Silicon Monolithic Integrated Circuits in RF Systems, Digest of Papers, pp. 107-110, Jan 2006.

[2] HA, M., and KWON, Y., "Ku-Band stop filter implemented on high resistivity silicon with inverted microstrip line photonic bandgap (PBG) structure," IEEE Microwave and Guided Wave Letters, pp.410-412, June 2005.

[3] WEIL, C., LUESSEM, G., and JAKOBY, R., "Tunable inverted-microstrip phase shifter device using nematic liquid crystals," IEEE MTT-S Int. Microwave Symp. Dig., Vol. 1, pp. 367-370, June 2002.

[4] MASUDA, TAKAHASHI, S., JOSHIN, T., and K., "An-over-110GHz InP HEMT flip-chip distributed baseband amplifier with inverted micrsotrip line structure for optical transmission system," IEEE Journal of Sold-State Circuits, Vol. 38, No. 9, pp. 1479-1484, Sep. 2003.

[5] YAMAGUCHI, S., IMAI, Y., SHIBATA, T., OTSUJI, T., HIRANO, M., and SANO, E., "An inverted microstrip line IC structure for ultra high-speed applications," IEEE MTT-S Int. Microwave Symp. Dig., Vol. 3, pp. 1643-1646, May 1995.

[6] POZAR, D. M., Microwave Engineering. John Wiley & Sons, Inc., 2005.

[7] PONCHAK, G. E., MARGOMENOS, A., KATEHI, L. P. B., "Low Loss, Finite Width Ground Plane, Thin Film Microstrip Lines on Si Wafers," Topical Meetings on Silicon Monolithic Integrated circuits in RF Systems, Digest of Papers, pp. 43-47, April. 2000.

[8] E. J. Derdinger, "A frequency dependent solution for microstrip transmission lines"; IEEE Trans. Microwave Theory Tech., vol. MTT-19, pp. 30-39, Jan. 1971.

[9] H. Cory, "Dispersion characteristics of microstrip lines"; IEEE Trans. Microwave Theory Tech., vol. MTT-29, pp. 59-61, Jan. 1981.

[10] TENTZERIS, E., KRUMPHOLZ, M., DIB, N., YOOK, J., and LINDA, P.B.K.,"FDTD Characterization of Waveguide-Probe Structures," IEEE Trans. Microwave Theory Tech., Vol. 46, No. 10, pp. 1452-1460, Oct. 1998.

[11] YEE, K.S., "Numerical solution of initial boundary value problems involving Maxwell's equations in isotropic media," IEEE Trans. Antennas Propagat., Vol. AP-14, pp. 302-307, May 1996.

[12] XIAO, S., VAHLDIECK, Jin R., and H., "Full-Wave Analysis of guided wave structures using a novel 2-D FDTD," IEEE Microwave and Guided Wave Letters, May 1992, pp. 165-167.

[13] PONCHAK, G.E., TENTZERIS, E.M. and PAPAPOLYMEROU, J., "Coupling Between Microstrip Lines Embedded in Polyimide Layers for 3D-MMICs on Si," Proc. of the 2001 International Microwave Symposium, Phoenix, AZ, May 2001, pp.1723-1726.

[14] WILLIAMS, D.F., OLYSLAGER, F., "Modal Cross Power in Quasi-TEM Transmission Lines," IEEE Microwave and Guided Wave Letters, November 1996, pp.413-415.